Controlled Synthesis of a Vacancy-Defect Single-Atom Catalyst for Boosting CO₂ Electroreduction

Xin Rong+, Hong-Juan Wang+, Xiu-Li Lu,* Rui Si,* and Tong-Bu Lu*

Abstract: *The reaction of precursors containing both nitrogen and oxygen atoms with Ni^{II} under 500°C can generate a N/O mixing coordinated $Ni-N_3O$ single-atom catalyst (SAC) in which the oxygen atom can be gradually removed under high temperature due to the weaker Ni—O interaction, resulting in a vacancy-defect $Ni-N_3$-V SAC at Ni site under 800°C. For the reaction of Ni^{II} with the precursor simply containing nitrogen atoms, only a no-vacancy-defect $Ni-N_4$ SAC was obtained. Experimental and DFT calculations reveal that the presence of a vacancy-defect in $Ni-N_3$-V SAC can dramatically boost the electrocatalytic activity for CO_2 reduction, with extremely high CO_2 reduction current density of 65 mA cm^{-2} and high Faradaic efficiency over 90% at −0.9 V vs. RHE, as well as a record high turnover frequency of 1.35×10^5 h^{-1}, much higher than those of $Ni-N_4$ SAC, and being one of the best reported electrocatalysts for CO_2-to-CO conversion to date.*

The excessive emission of CO₂ from continuous consumption of fossil fuels has triggered serious environmental issues.[1,2] Electrocatalytic CO₂ reduction has been considered as a promising and clean approach to decrease the atmospheric concentration of CO₂ greenhouse gas through the conversion of CO₂ into valuable carbonaceous products.[3–6] For industrial application of electrocatalytic CO₂ reduction, both high current density and high Faradaic efficiency are essential. However, the Faradaic efficiencies usually drop rapidly along with the increase of overpotentials for achieving high current densities, due to the competing reaction of hydrogen reduction.[7–14] There is still difficult for achieving high Faradaic efficiency at high current density, and only few electrocatalysts display high current density and high Faradaic efficiency simultaneously.[15–17]

Recently, single atomically dispersed catalysts (also called single-atom-catalysts, SACs) have been drawn much attention in heterogeneous catalysis, which is due to their 100% atomic utilization efficiency, as well as their outstanding catalytic performance in water splitting,[18–21] oxygen reduction,[22,23] CO₂ reduction,[9–12,14–17,24,25] and other heterogeneous catalytic reactions.[26–28] Many factors can affect the catalytic performance of SACs. Besides the supports, the loading amount and coordination numbers of SACs, the defects on the support have also been found to be a tunable factor for optimizing the catalytic performance of SACs, through inducing different local electronic densities of state of metals.[29,30] However, controlling the positions and numbers of defects on the supports during the synthesis of SACs remain great challenge, and it still lacks efficient strategy for control synthesis of such SACs.

Herein, we report a facile strategy for control synthesis of a vacancy-defect Ni SAC, using the precursors of cyanuric acid (CA) and 2,4-diamino-6-phenyl-1,3,5-triazine (DPT) based on the following considerations: 1) Both oxygen and nitrogen atoms in CA and DPT (Figure 1a) can coordinate to Ni^{II} to form O/N mixed coordinated geometry, in which the coordinated oxygen atom can be primarily removed under high temperature (800°C) due to the weaker Ni-O coordination bond (compared with Ni—N bond), potentially resulting in a vacancy-defect at single Ni atom site (Figure 1a); 2) it is worth noting that the mixed precursors of CA and DPT go through a melting process before pyrolysis (Supporting Information, Figure S1), thus it can be easily and strongly coated the vacancy-defect SACs on any conductive substrates, such as carbon cloth, metal foils, or metal foams (Supporting Information, Figure S2). Using the above strategy, we easily obtained a vacancy-defect Ni SAC (named as Ni-N₃-V) on the surface of carbon cloth. The state-of-the-art Ni-N₃-V SAC displays excellent electrocatalytic performance for CO₂-to-CO conversion, with both high current density of 65 mA cm^{-2} and high Faradaic efficiency over 90% at −0.9 V vs. RHE, as well as a record high turnover frequency of 1.35×10^5 h^{-1}. The general strategy for the control synthesis of vacancy-defect SACs presented herein will boost the development of highly efficient heterogeneous catalysts towards various catalysis, and deeply understand the vacancy defects on the catalytic performance of SACs.

The Ni-N₃-V SAC was prepared by heating a mixture of CA, DPT, and NiCl₂·6H₂O under an N₂ atmosphere (Figure 1a). Firstly, the solids of the above three precursors were stirred in deionizer water for 6 h, and subsequently dried in vacuum for 12 h. The obtained mixture was heated with a piece of carbon cloth under an N₂ atmosphere. When the temperature was increased to 460°C, the solid mixture turned into a yellow liquid (Supporting Information, Figure S1), which can be strongly and uniformly coated on the carbon cloth. Upon further heating to 500°C, N/O mixing coordinated Ni-N₃O SACs were formed within 2D carbon nano-

[*] X. Rong,[+] Dr. H. J. Wang,[+] Dr. X. L. Lu, Prof. T. B. Lu
Institute for New Energy Materials & Low Carbon Technologies,
School of Materials Science and Engineering
Tianjin University of Technology, Tianjin 300384 (China)
E-mail: luxiuli@email.tjut.edu.cn
        lutongbu@tjut.edu.cn

Prof. R. Si
Shanghai Synchrotron Radiation Facility, Shanghai Institute of
Applied Physics, Chinese Academy of Sciences
Shanghai 201204 (China)
E-mail: sirui@sinap.ac.cn

[+] These authors contributed equally to this work.

Supporting information and the ORCID identification number(s) for the author(s) of this article can be found under:
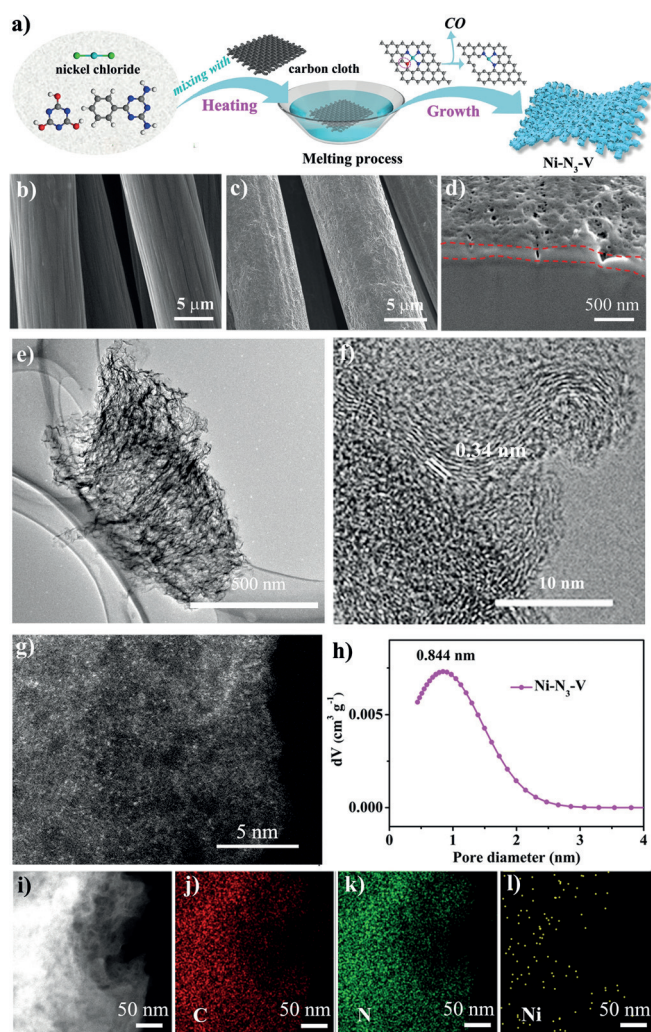https://doi.org/10.1002/anie.201912458.

Figure 1. a) Illustration for the synthesis of Ni-N$_3$-V. b),c) SEM images for the carbon cloth before (b) and after (c) coating Ni-N$_3$-V. d) SEM image for the cross section of Ni-N$_3$-V grown on the carbon cloth. e)–g) TEM image (e,f) and HAADF-STEM image (g) for Ni-N$_3$-V, showing the lattice fringes of graphitic carbon (f) and Ni single atoms (bright dots in (g) in Ni-N$_3$-V. h) The pore diameter distribution for Ni-N$_3$-V obtained by nitrogen adsorption isotherm. i)–l) HAADF-STEM image (i) and element mapping (j–l) for Ni-N$_3$-V.

sheets (Figure 1 a), in which the coordinated oxygen atom together with the connected carbon atom can be primarily removed by releasing a CO molecule at high temperature (500–800 °C), generating a vacancy-defect Ni-N$_3$-V SAC at 800 °C (Figure 1 a). While the reaction of DPT with Ni^{II} at 800 °C can only obtain a no-vacancy-defect Ni-N$_4$ SAC, though the mixed precursors of NiCl$_2$·6 H$_2$O with DPT also go through a melting process before pyrolysis (Supporting Information, Figure S3). This provides an ideal strategy for large-scale control synthesis of vacancy-defect SACs firmly coating on any conducting substrate, such as carbon cloth, copper foam or titanium foil (Supporting Information, Figure S2), which can be used directly as an electrode without requiring extra glues to stick SACs onto the surface of conducting substrate. Such a facile strategy for large-scale synthesis of SACs on any conducting substrate is beneficial for industrial applications.

The microstructure of Ni-N$_3$-V was investigated by scanning electron microscopy (SEM), transition electron microscopy (TEM), and high-angle annular dark-field scanning transmission electron microscopy (HAADF-STEM). As shown in Figures 1 b and c, the SEM images indicate the surface of carbon cloth becomes rough after coating Ni-N$_3$-V. The cross-sectional SEM image (Figure 1 d) and corresponding element mapping (Supporting Information, Figure S4) confirm the growth of Ni-N$_3$-V layer on the carbon cloth, with the thickness of about 200 nm. Furthermore, Ni-N$_3$-V shows a nanosheet morphology with numerous wrinkles (Figure 1 e), and a large BET-surface area of 126 m^{2}g^{-1} with well CO$_2$ adsorption ability (Supporting Information, Figure S5). The high-resolution TEM image exhibits obvious lattice fringes with spacing of 0.34 nm (Figure 1 f), which can be assigned to the (002) plane of graphitic carbon.[31] Furthermore, the HAADF-STEM image of Ni-N$_3$-V shows abundant pores, as noted by red circles in the Supporting Information, Figure S6. The size of the pores is about 1 nm, corresponding well with the pore diameter distributions obtained from N$_2$ sorption isotherm (Figure 1 h). Moreover, the atomic resolution HAADF-STEM image (Figure 1 g) also confirms the existence of pores (Supporting Information, Figure S6), as well as abundant isolated Ni single atoms. The element mapping of Ni-N$_3$-V (Figures 1 i–l) shows the uniform distribution of C, N, and Ni elements, demonstrating the successful synthesis of atomically dispersed nickel atoms on vacancy-defect-rich N-doped graphitic carbon. Similar to Ni-N$_3$-V, Ni-N$_4$ can be also uniformly coated on the surface of carbon cloth through a melting process (Supporting Information, Figure S7a), with the thickness of about 200 nm (Supporting Information, Figure S7b). Moreover, the atomic resolution HAADF-STEM image (Supporting Information, Figure S8a) confirms that the Ni atoms in Ni-N$_4$ are also atomically dispersed, with the uniform distribution of C, N, and Ni elements (Supporting Information, Figure S8b).

The electronic and structural information of Ni atoms in Ni-N$_3$-V and Ni-N$_4$ were investigated by X-ray absorption fine structure (XAFS) spectroscopy. As shown in Figure 2 a, the energy of pre-edge in X-ray absorption near edge structure (XANES) curves for Ni-N$_3$-V and Ni-N$_4$ are higher than that of Ni foil and lower than that of NiO, indicating the Ni atoms have positive charges of Ni$^{δ+}$ ($0 < δ < 2$) in Ni-N$_3$-V and Ni-N$_4$. Furthermore, as demonstrated by Fourier transformations-extended X-ray fine structure (FT-EXAFS) spectra in Figure 2 b, Ni-N$_3$-V and Ni-N$_4$ display the main peaks around 1.86 Å, which can be assigned to the Ni−N bonds,[32] as this distance is close to that of NiPc, and shorter than that of Ni(acac)$_2$ (Supporting Information, Figure S9). The absence of a Ni−Ni peak at about 2.5 Å confirms the isolated dispersion of Ni atoms on N-doped graphitic carbon for both Ni-N$_3$-V and Ni-N$_4$. To identify the coordination environment around Ni atom, the FT-EXAFS of Ni-N$_3$-V and Ni-N$_4$ were fitted in R space. The fitting curves accord well with the experimental curves (Supporting Information, Figure S10), and the results show that each Ni atom is coordinated by three nitrogen atoms for Ni-N$_3$-V and four nitrogen atoms for Ni-N$_4$, respectively (Supporting Information, Table S1). Moreover, the Ni−N distance in Ni-N$_3$-V
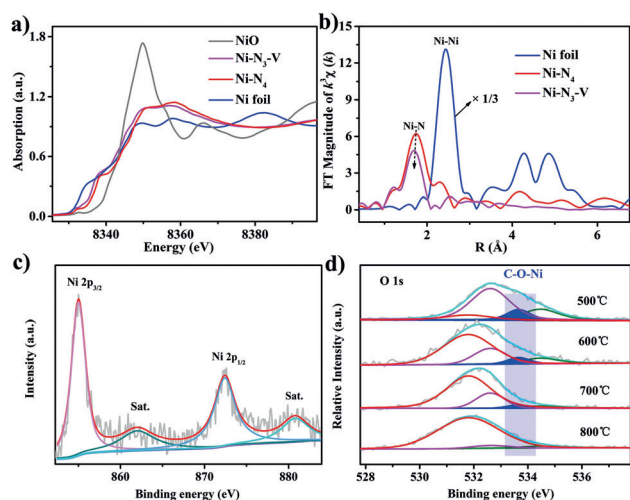
Figure 2. a) Ni K-edge XANES profiles for Ni-N$_3$-V, Ni-N$_4$, Ni foil and NiO. b) Ni K-edge k^3-weighted FT-EXAFS spectra of Ni-N$_3$-V, Ni-N$_4$, and Ni foil (the EXAFS intensity of Ni foil is shown at one third value). c) Ni 2p XPS of Ni-N$_3$-V. d) O 1s XPS of the samples obtained at 500 (Ni-N$_3$O), 600, 700 and 800°C (Ni-N$_3$-V).

(1.84(1) Å) is slightly shorter than that in Ni-N$_4$ (1.88(1) Å; Supporting Information, Table S1), indicating the stronger Ni−N coordination interactions in Ni-N$_3$-V.

To further understand the electronic state and coordination environment of Ni sites in Ni-N$_3$-V, the X-ray photoelectron spectroscopy (XPS) measurements were conducted. As shown in Figure 2c, the binding energy position of Ni 2p$_{3/2}$ in Ni-N$_3$-V is 855.0 eV, which is higher than that of Ni^0 (853.5 eV) and lower than that of Ni^{2+} (855.8 eV),[17] further demonstrating the valence state of Ni is between 0 and 2. This low-valent Ni atom in SACs has been considered as the highly active sites for CO$_2$ electroreduction due to partially occupied 3d orbital.[17] The high-resolution XPS of N 1s for Ni-N$_3$-V can be deconvoluted into six subpeaks located at 398.1, 398.9, 399.4, 400.5, 401.3, and 403.0 eV, respectively (Supporting Information, Figure S11), which can be assigned to the pyridinic-N, Ni−N (pyridinic-N), pyrrolic-N, graphitic-N, quaternary-N, and oxidized-N, respectively (Supporting Information, Table S2). In NC, however, no subpeak at 398.9 eV belonging to Ni−N species can be observed (Supporting Information, Figure S11). The above difference indicates the existence of Ni−N species in Ni-N$_3$-V. Moreover, the high-resolution XPS of C 1s indicate the patterns of Ni-N$_3$-V and NC are almost identical (Supporting Information, Figure S12), further demonstrating the Ni atoms in Ni-N$_3$-V are coordinated to N rather than C atoms. To further investigate the formation process of Ni-N$_3$-V, the coordination environment of Ni atoms in Ni-N$_3$O was investigated by FT-EXAFS. As exhibited in the Supporting Information, Figures S7a,d and Table S1, the Ni atoms in Ni-N$_3$O are coordinated by four nitrogen or oxygen atoms. Although we cannot definitely distinguish Ni−N and Ni−O bonds, the average Ni−N/O distance in Ni-N$_3$O is 1.88(1) Å, which are close to the Ni−N distances in Ni-N$_4$ and NiPc (Ni−N), and shorter than Ni−O distance in Ni(acac)$_2$ (Supporting Information, Figure S9), indicating the main species in Ni-N$_3$O is N rather O.

Furthermore, the O 1s XPS data for Ni-N$_3$O and the samples obtained at 600, 700 and 800°C were further measured. As shown in Figure 2d, the O 1s XPS for Ni-N$_3$O shows four subpeaks located at 531.8, 532.6, 533.6, and 534.4 eV, respectively, which can be attributed to the O species from O= C$_{aromatic}$, O−C$_{aromatic}$, Ni−O−C$_{aromatic}$, and adsorbed water, respectively.[33] While only two subpeaks located at 532.6 and 534.4 eV can be observed for the sample obtained by the reaction of NiCl$_2$·6H$_2$O with DPT at 500°C (Supporting Information, Figure S13), the absence of Ni−O−C$_{aromatic}$ subpeak demonstrate Ni-N$_3$O cannot be formed in the absence of CA. Notably, the intensities of subpeak located at 533.6 eV belonging to Ni−O−C$_{aromatic}$ decrease along with increasing temperature, and almost disappear at 800°C (Figure 2d), which can be attributed to gradually transformation from Ni-N$_3$O to Ni-N$_3$-V, through removing the coordinated Ni−O−C$_{aromatic}$ in NiON$_3$ with increasing temperature, owing to the weaker Ni-O coordination bond (compared with Ni−N bond), as the Ni−O bond length is longer than the Ni−N bond length (Supporting Information, Figures S6 and S11). Indeed, CO can be detected by the in situ IR spectra during heating Ni-N$_3$O from 500 to 700°C (Supporting Information, Figure S14), confirming the conversion process from Ni-N$_3$O to Ni-N$_3$-V (Figure 1a).

The CO$_2$ electrocatalytic activities of Ni-N$_3$-V, Ni-N$_4$, and NC were investigated in a three-electrode system containing CO$_2$-saturated 0.5 M KHCO$_3$ as electrolyte. As shown by the linear sweep voltammetry (LSV) in Figure 3a, Ni-N$_3$-V displays extremely high electrocatalytic activity for CO$_2$ reduction, achieving a current density of 65 mA cm^{-2} at −0.9 V vs. RHE, with a slow scan rate of 1 mV s^{-1}, this value is much larger than those of Ni-N$_4$ (19 mA cm^{-2}) and NC (12 mA cm^{-2}), and also larger than those of most reported CO$_2$ reduction electrocatalysts (Supporting Information, Table S3), demonstrating that Ni-N$_3$-V is one of the best reported electrocatalysts for CO$_2$-to-CO conversion to date.
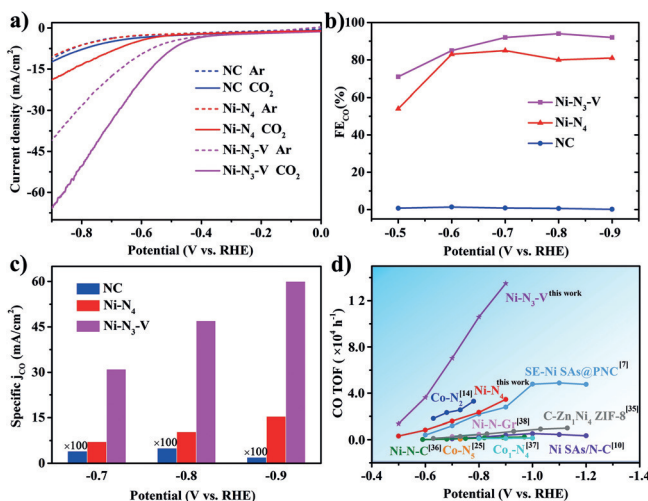

Figure 3. a) Linear sweep voltammetric curves in N$_2$ or CO$_2$-saturated 0.5 M KHCO$_3$ electrolyte, with a scan rate of 1 mV s^{-1}, and a stirring rate of 550 rpm using a magnetic stirring bar. b) Faradaic efficiencies for CO. c) Specific current density of CO for Ni-N$_3$-V, Ni-N$_4$ and NC (the value for NC is shown times 100). d) TOFs of Ni-N$_3$-V and Ni-N$_4$ for CO compared with those of other state-of-the-art SACs.

To rationally compare the catalytic activity of Ni-N_3-V and Ni-N_4, their current densities were normalized to the mA/$\mu g_{Ni} cm^2$. The mass activities of Ni-N_3-V are over four times than those of Ni-N_4 at -0.7---0.9 V vs. RHE (Supporting Information, Figure S15), demonstrating the enhanced catalytic activity of Ni-N_3-V origins from its vacancy-defect rather than the different loading of Ni. Furthermore, the electrocatalytic performance of as-prepared samples with CA/DPT ration of 0.5, 1.5, and 2.0 were also measured, and compared with those of Ni-N_4 (CA/DPT = 0) and Ni-N_3-V (CA/DPT = 1.0). Ni-N_3-V shows the best catalytic performance (Supporting Information, Figure S16), though the density of defect sites determined by the Raman spectra[8] increase linearly with increasing CA/DPT ratio (Supporting Information, Figure S16a).

Controlled potential electrolysis was conducted to evaluate the Faradaic efficiencies (FEs) of the catalysts. The results show that CO and H_2 are the dominant reduction products, and no liquid product was detected by ^{1}H NMR spectroscopy (Supporting Information, Figure S17). As shown in Figure 3b, the Faradaic efficiencies for CO production is over 90% under the potentials ranging from -0.7 to -0.9 V, with a maximum FE of 94% at -0.8 V, while Ni-N_4 and NC shows FEs of only around 85% and 0.6% under the same potential range. The Tafel slope value for Ni-N_3-V (124 mV dec^{-1}) is also much smaller than those of Ni-N_4 (470 mV dec^{-1}) and NC (588 mV dec^{-1}; Supporting Information, Figure S18a), suggesting the favorable kinetics of Ni-N_3-V for the reduction of CO_2. Moreover, the results of the electrochemical impedance spectroscopy (EIS) indicate that Ni-N_3-V possesses much lower charge-transfer resistance than Ni-N_4 and NC (Supporting Information, Figure S18b), benefiting the electrochemical reduction of CO_2. The specific current densities of CO for Ni-N_3-V, Ni-N_4, and NC were calculated at -0.7, -0.8, and -0.9 V (Figure 3c), demonstrating both high activity and selectivity of Ni-N_3-V for CO_2 reduction. To confirm the catalytic active sites in Ni-N_3-V, SCN$^-$ anion was applied as an indicator to poison the Ni atoms. As shown in the Supporting Information, Figure S19, the current density of Ni-N_3-V is obviously suppressed after the addition of SCN$^-$, validating the single atomically dispersed Ni is the main active site for CO_2 reduction.[34] The turnover frequencies (TOF) for CO_2 reduction normalized to single Ni sites were calculated (Supporting Information, Figure S18c), of which Ni-N_3-V possesses a record high TOF value of 1.35×10^5 h^{-1} at -0.90 V, much higher than those of Ni-N_4 (3.46×10^4 h^{-1}), it is also obviously higher than those of reported state-of-the-art SACs measured under similar conditions (Figure 3d).[7,10,14,25,35–38] Besides high Faradaic efficiency and high TOF value at high current density, Ni-N_3-V also exhibits long time stability, retaining 95% of the initial current density after 14 h electrolysis (Supporting Information, Figure S18d), holding great potential for industrial application in electrocatalytic CO_2 reduction.

To further understand the origin of the outstanding catalytic performance of Ni-N_3-V for CO_2 reduction, DFT calculations were carried out. As exhibited in Figure 4a, three optimized structures of Ni SACs, including Ni-N_4, Ni-N_3, and Ni-N_3-V are used as the models for calculations (Supporting
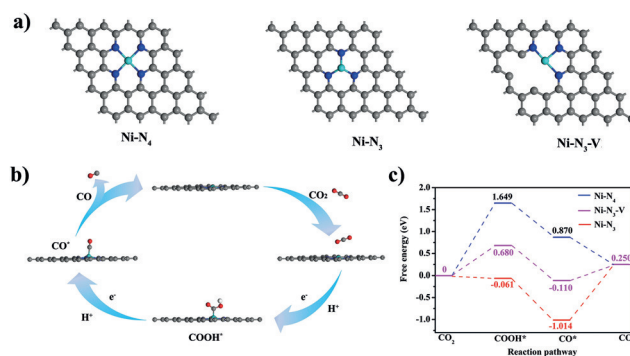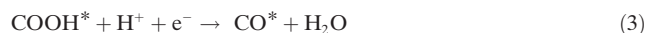

Figure 4. a) Three optimized structures of Ni SACs. b) The proposed reaction paths of Ni-N_3-V for CO_2 electroreduction to CO. c) Calculated free-energy diagram for the conversion of CO_2 to CO.

Information, Figure S20). The reaction paths for CO_2 electroreduction to CO are known to encompass the following four elementary steps (Figure 4b):

$$CO_2 + * \rightarrow CO_2* \; (* = catalytic \; site) \tag{1}$$

$$CO_2* + H^+ + e^- \rightarrow COOH* \tag{2}$$

$$COOH* + H^+ + e^- \rightarrow CO* + H_2O \tag{3}$$

$$CO* \rightarrow CO + * \tag{4}$$

in which the reduction of CO_2 to COOH* is generally regarded as the rate-limiting step.[39] The reaction free energies are shown in Figure 4c. For the total energies of the first and second steps, Ni-N_4, Ni-N_3-V, and Ni-N_3 exhibit the free energies of 1.649, 0.680, and -0.061 eV, respectively, indicating Ni-N_3 possesses the most favorable ΔG in this step. After that, all of the three catalysts could easily realize the transformation of COOH* species to CO*, owing to their downhill free energy profiles. However, at the fourth step, Ni-N_3 shows difficulty to release CO from its active site, as the calculated free energy ($\Delta G = 1.264$ eV) is the largest among the three catalysts, indicating that Ni-N_3 without a vacancy is not an efficient SAC for CO_2 reduction.[40] Given all this, it is expected that Ni-N_3-V displays the highest electrocatalytic activity for CO_2 reduction owing to its optimizing and moderate ΔG values for CO_2 activation and CO desorption.

In summary, we have developed a facile method for control synthesis of vacancy-defect Ni-N_3-V SAC on conducting substrate, by using the precursors containing both oxygen and nitrogen atoms, in which the oxygen atom in initially formed Ni-N_3O can be removed under high temperature to generate a vacancy-defect Ni-N_3-V. The Ni-N_3-V SAC shows outstanding electrocatalytic performance for CO_2 reduction, achieving high current density (65 mA cm^{-2}) and high Faradaic efficiency (over 90%) simultaneously for CO evolution at -0.9 V vs. RHE, as well as a record turnover frequency of 1.35×10^5 h^{-1}. The results of experimental and DFT calculations revealed that the presence of a vacancy defect at the Ni-N_3 site plays a key role for boosting the CO_2 electroreduction, which can lower the energy barriers for the formation of COOH* intermediate and desorption of CO. Our work opens a new window for control synthesis of

1964 www.angewandte.org

© 2020 Wiley-VCH Verlag GmbH & Co. KGaA, Weinheim

Angew. Chem. Int. Ed. **2020**, *59*, 1961–1965

vacancy-defect SACs to engineer and optimize the coordination environments and electronic structures of SACs to enhance their catalytic activity.

Conflict of interest

The authors declare no conflict of interest.

[1] C. W. Li, J. Ciston, M. W. Kanan, *Nature* **2014**, *508*, 504.
[2] J. Qiao, Y. Liu, F. Hong, J. Zhang, *Chem. Soc. Rev.* **2014**, *43*, 631–675.
[3] S. Gao, Y. Lin, X. Jiao, Y. Sun, Q. Luo, W. Zhang, D. Li, J. Yang, Y. Xie, *Nature* **2016**, *529*, 68.
[4] Y. Zheng, A. Vasileff, X. Zhou, Y. Jiao, M. Jaroniec, S.-Z. Qiao, *J. Am. Chem. Soc.* **2019**, *141*, 7646–7659.
[5] M. Schreier, F. Héroguel, L. Steier, S. Ahmad, J. S. Luterbacher, M. T. Mayer, J. Luo, M. Grätzel, *Nat. Energy* **2017**, *2*, 17087.
[6] a) A. Vasileff, Y. Zheng, S. Z. Qiao, *Adv. Energy Mater.* **2017**, *7*, 1700759; b) P. Chen, Y. Jiao, Y.-H. Zhu, S. M. Chen, L. Song, M. Jaroniec, Y. Zheng, S. Z. Qiao, *J. Mater. Chem. A* **2019**, *7*, 7675–7682; c) A. Vasileff, C. Xu, Y. Jiao, Y. Zheng, S. Z. Qiao, *Chem* **2018**, *4*, 1809–1831.
[7] J. Yang, Z. Qiu, C. Zhao, W. Wei, W. Chen, Z. Li, Y. Qu, J. Dong, J. Luo, Z. Li, Y. Wu, *Angew. Chem. Int. Ed.* **2018**, *57*, 14095–14100; *Angew. Chem.* **2018**, *130*, 14291–14296.
[8] W. Ju, A. Bagger, G.-P. Hao, A. S. Varela, I. Sinev, V. Bon, B. Roldan Cuenya, S. Kaskel, J. Rossmeisl, P. Strasser, *Nat. Commun.* **2017**, *8*, 944.
[9] X. Zu, X. Li, W. Liu, Y. Sun, J. Xu, T. Yao, W. Yan, S. Gao, C. Wang, S. Wei, Y. Xie, *Adv. Mater.* **2019**, *31*, 1808135.
[10] C. Zhao, X. Dai, T. Yao, W. Chen, X. Wang, J. Wang, J. Yang, S. Wei, Y. Wu, Y. Li, *J. Am. Chem. Soc.* **2017**, *139*, 8078–8081.
[11] K. Jiang, S. Siahrostami, A. J. Akey, Y. Li, Z. Lu, J. Lattimer, Y. Hu, C. Stokes, M. Gangishetty, G. Chen, Y. Zhou, W. Hill, W.-B. Cai, D. Bell, K. Chan, J. K. Nørskov, Y. Cui, H. Wang, *Chem* **2017**, *3*, 950–960.
[12] F. Yang, P. Song, X. Liu, B. Mei, W. Xing, Z. Jiang, L. Gu, W. Xu, *Angew. Chem. Int. Ed.* **2018**, *57*, 12303–12307; *Angew. Chem.* **2018**, *130*, 12483–12487.
[13] X.-M. Hu, H. H. Hval, E. T. Bjerglund, K. J. Dalgaard, M. R. Madsen, M.-M. Pohl, E. Welter, P. Lamagni, K. B. Buhl, M. Bremholm, M. Beller, S. U. Pedersen, T. Skrydstrup, K. Daasbjerg, *ACS Catal.* **2018**, *8*, 6255–6264.
[14] X. Wang, Z. Chen, X. Zhao, T. Yao, W. Chen, R. You, C. Zhao, G. Wu, J. Wang, W. Huang, J. Yang, X. Hong, S. Wei, Y. Wu, Y. Li, *Angew. Chem. Int. Ed.* **2018**, *57*, 1944–1948; *Angew. Chem.* **2018**, *130*, 1962–1966.
[15] J. Gu, C.-S. Hsu, L. Bai, H. M. Chen, X. Hu, *Science* **2019**, *364*, 1091–1094.
[16] C. Zhao, Y. Wang, Z. Li, W. Chen, Q. Xu, D. He, D. Xi, Q. Zhang, T. Yuan, Y. Qu, J. Yang, F. Zhou, Z. Yang, X. Wang, J. Wang, J. Luo, Y. Li, H. Duan, Y. Wu, Y. Li, *Joule* **2019**, *3*, 584–594.
[17] H. B. Yang, S.-F. Hung, S. Liu, K. Yuan, S. Miao, L. Zhang, X. Huang, H.-Y. Wang, W. Cai, R. Chen, J. Gao, X. Yang, W. Chen, Y. Huang, H. M. Chen, C. M. Li, T. Zhang, B. Liu, *Nat. Energy* **2018**, *3*, 140–147.
[18] H. Fei, J. Dong, Y. Feng, C. S. Allen, C. Wan, B. Volosskiy, M. Li, Z. Zhao, Y. Wang, H. Sun, P. An, W. Chen, Z. Guo, C. Lee, D. Chen, I. Shakir, M. Liu, T. Hu, Y. Li, A. I. Kirkland, X. Duan, Y. Huang, *Nat. Catal.* **2018**, *1*, 63–72.
[19] Y. Xue, B. Huang, Y. Yi, Y. Guo, Z. Zuo, Y. Li, Z. Jia, H. Liu, Y. Li, *Nat. Commun.* **2018**, *9*, 1460.
[20] X. P. Yin, H. J. Wang, S. F. Tang, X. L. Lu, M. Shu, R. Si, T. B. Lu, *Angew. Chem. Int. Ed.* **2018**, *57*, 9382–9386; *Angew. Chem.* **2018**, *130*, 9526–9530.
[21] Z. Zhang, Y. Chen, L. Zhou, C. Chen, Z. Han, B. Zhang, Q. Wu, L. Yang, L. Du, Y. Bu, P. Wang, X. Wang, H. Yang, Z. Hu, *Nat. Commun.* **2019**, *10*, 1657.
[22] Y. Zheng, Y. Jiao, Y. Zhu, Q. Cai, A. Vasileff, L. H. Li, Y. Han, Y. Chen, S. Z. Qiao, *J. Am. Chem. Soc.* **2017**, *139*, 3336–3339.
[23] P. Chen, T. Zhou, L. Xing, K. Xu, Y. Tong, H. Xie, L. Zhang, W. Yan, W. Chu, C. Wu, Y. Xie, *Angew. Chem. Int. Ed.* **2017**, *56*, 610–614; *Angew. Chem.* **2017**, *129*, 625–629.
[24] Y. Chen, S. Ji, C. Chen, Q. Peng, D. Wang, Y. Li, *Joule* **2018**, *2*, 1242–1264.
[25] Y. Pan, R. Lin, Y. Chen, S. Liu, W. Zhu, X. Cao, W. Chen, K. Wu, W. C. Cheong, Y. Wang, L. Zheng, J. Luo, Y. Lin, Y. Liu, C. Liu, J. Li, Q. Lu, X. Chen, D. Wang, Q. Peng, C. Chen, Y. Li, *J. Am. Chem. Soc.* **2018**, *140*, 4218–4221.
[26] A. Wang, J. Li, T. Zhang, *Nat. Rev. Chem.* **2018**, *2*, 65–81.
[27] Z. Li, D. Wang, Y. Wu, Y. Li, *Nat. Sci. Rev.* **2018**, *5*, 673–689.
[28] X. Guo, G. Fang, G. Li, H. Ma, H. Fan, L. Yu, C. Ma, X. Wu, D. Deng, M. Wei, D. Tan, R. Si, S. Zhang, J. Li, L. Sun, Z. Tang, X. Pan, X. Bao, *Science* **2014**, *344*, 616–619.
[29] X. Yan, X. Jia, X. Yao, *Chem. Soc. Rev.* **2018**, *47*, 7628–7658.
[30] D. Li, Y. Jia, G. Chang, J. Chen, H. Liu, J. Wang, Y. Hu, Y. Xia, D. Yang, X. Yao, *Chem* **2018**, *4*, 2345–2356.
[31] H. Tan, Y. Li, J. Kim, T. Takei, Z. Wang, X. Xu, J. Wang, Y. Bando, Y.-M. Kang, J. Tang, Y. Yamauchi, *Adv. Sci.* **2018**, *5*, 1800120.
[32] W. Bi, X. Li, R. You, M. Chen, R. Yuan, W. Huang, X. Wu, W. Chu, C. Wu, Y. Xie, *Adv. Mater.* **2018**, *30*, 1706617.
[33] A. Ganguly, S. Sharma, P. Papakonstantinou, J. Hamilton, *J. Phys. Chem. C* **2011**, *115*, 17009–17019.
[34] X. Li, W. Bi, M. Chen, Y. Sun, H. Ju, W. Yan, J. Zhu, X. Wu, W. Chu, C. Wu, Y. Xie, *J. Am. Chem. Soc.* **2017**, *139*, 14889–14892.
[35] C. Yan, H. Li, Y. Ye, H. Wu, F. Cai, R. Si, J. Xiao, S. Miao, S. Xie, F. Yang, Y. Li, G. Wang, X. Bao, *Energy Environ. Sci.* **2018**, *11*, 1204–1210.
[36] F. Pan, W. Deng, C. Justiniano, Y. Li, *Appl. Catal. B* **2018**, *226*, 463–472.
[37] Z. Geng, Y. Cao, W. Chen, X. Kong, Y. Liu, T. Yao, Y. Lin, *Appl. Catal. B* **2019**, *240*, 234–240.
[38] P. Su, K. Iwase, S. Nakanishi, K. Hashimoto, K. Kamiya, *Small* **2016**, *12*, 6083–6089.
[39] H. A. Hansen, J. B. Varley, A. A. Peterson, J. K. Nørskov, *J. Phys. Chem. Lett.* **2013**, *4*, 388–392.
[40] Y. Jiao, Y. Zheng, P. Chen, M. Jaroniec, S.-Z. Qiao, *J. Am. Chem. Soc.* **2017**, *139*, 18093–18100.